

Fingerprinting soft material nanostructure response to complex flow histories

Patrick T. Corona,¹ Barbara Berke¹,² Manuel Guizar-Sicairos^{1,3}, L. Gary Leal,¹
Marianne Liebi,^{2,*} and Matthew E. Helgeson^{1,†}

¹University of California, Santa Barbara, Department of Chemical Engineering Santa Barbara, California 93106, USA

²Department of Physics, Chalmers University of Technology, SE-412 96 Gothenburg, Sweden

³Swiss Light Source, Paul Scherrer Institut, 5232 Villigen PSI, Switzerland



(Received 25 February 2021; accepted 21 March 2022; published 25 April 2022)

Understanding the complex connection between flow-processing history, fluid structure, and fluid properties represents a grand challenge for the engineering and fundamental study of nanostructured soft materials. To address this challenge, we report measurements using scanning small-angle x-ray scattering in a fluidic four-roll mill (FFoRM), which enables rapid nanostructural characterization of complex fluids under an unprecedentedly diverse range of flow histories. Combining this technique with analysis of the Lagrangian deformation history of fluid elements, we demonstrate rapid mapping of orientational ordering of fluids' nanostructure along diverse deformation trajectories that emulate those encountered in flow processing. Using demonstrative experiments on model rodlike nanoparticle dispersions, we show that differences in rod flexibility and rod-rod interactions play a significant role in determining the fluid's anisotropic structural response to similar flow histories. An analysis of the coupling between measured particle alignment and interparticle correlations reveals these differences to arise from the nature and strength of interparticle interactions in flow. These measurement and analysis techniques produce large datasets that hold promise toward advancing process-structure-property models and inverse design processes of flows that are tailored to produce targeted nanostructures.

DOI: [10.1103/PhysRevMaterials.6.045603](https://doi.org/10.1103/PhysRevMaterials.6.045603)

I. INTRODUCTION

Fluids with complex structural responses to imposed flow fields are ubiquitous in the industrial production of many soft materials [1]. Complex fluids are subjected to diverse flow fields as they are convected through such processes, for example, extensional flows encountered in contractions/expansions or simple shear flows experienced in flow through straight pipes or channels. These processes use flow fields sufficient to produce out-of-equilibrium fluid microstructures that will be retained in the final processed material if the relaxation of the microstructure is slow compared to processing times. An example of such a process is blade coating, where the flow histories a fluid experiences depend on the fluid's distance from the interface and position relative to the moving blade. As a result, the fluid experiences both time-varying and spatially varying flows. In the blade coating of organic semiconductors, for example, crystallization processes simultaneously lock in the flow-induced material structure before it can relax, enabling one to tune the final structure of the semiconductor through the use of micropatterned blades [2,3]. Similarly, 3D printing via direct ink writing produces flow histories that vary depending on the location within the nozzle and the radial position within the printed filament [4,5]. Again, the variability in flows generated by the process result in both time- and spatially-varying flows that influence

the final printed structure and properties [6]. Determining process-structure-property relationships for such nonequilibrium structures represents a grand challenge in the field of soft matter. With enhanced understanding of these relationships one could better predict processing parameters, e.g., device geometries and power inputs required to process the fluid, as well as the onset of complications such as flow instabilities [7–10] for a fluid entering an existing process or design new processes to target a desired microstructure or flow response.

Conventionally, process-structure-property relationships for flowing soft materials are determined through the development and testing of micromechanically derived rheological models under well-defined flow histories [1,11,12]. Although its simplicity provides physical insight into material behavior, this approach potentially biases models towards flow histories that are more easily implemented in experiment and simulation, such as homogeneous simple shear and extensional flows. This presents a disconnect with flow histories encountered in real processes, which typically involve inhomogeneous and/or mixed flow types in which a Lagrangian material element following the flow encounters complex variations of flow strength and type in time. Furthermore, the derivation of such micromechanical models requires two components: a model for the evolution of the microstructure under a given flow history, i.e., a process-structure relationship, and a theory for the calculation of the stress, i.e., a structure-property relationship. A successful comparison between experimental measurements and rheological models requires that both aspects of the model are accurate. The problem is further complicated by the fact that changes to

*marianne.liebi@psi.ch

†helgeson@ucsb.edu

the fluid stress can change the flow fields, i.e., a property-process relationship, in the form of flow modification or flow instabilities. An alternative strategy could be to approach these three relationships separately, which would enable the testing of each model/theory component individually or the use of data-driven methods, such as machine learning, toward the design and testing of physical models. Regardless of the implementation, this alternative approach ultimately requires experimental datasets that are representative of the processing histories that fluids will encounter, which are not yet experimentally feasible to generate. In this work, we will present developed experimental and analysis methods that can be used to probe the nanostructure of complex fluids under a remarkably large set of flow histories to enable the rigorous testing of rheological models, as well as providing the dataset that could ultimately enable the computationally aided derivation of processing-structure models.

The development of instruments to probe complex fluid structure under complex flow histories was pioneered by Taylor, who developed the mechanical four-roll mill to study the deformation of droplets dispersed in a Newtonian fluid under controlled variable flow types [13]. The mechanical four-roll mill uses four rotating cylinders immersed in the fluid to control the flow fields in an idealized 2D homogeneous flow near a stagnation point, i.e., a region where the fluid velocity is zero but the rate of strain is nonzero. The four-roll mill design was later adapted for the measurement of complex fluid structure with birefringence and small-angle light scattering, which probe the alignment of the microstructure and larger scale (around 1 μm) microstructural features, respectively [14–16]. However, practical challenges related to scaling down its dimensions and sealing the device from leaks prevent the mechanically driven device from being implemented for use in small-angle x-ray or neutron scattering applications, which are more ideal measurement techniques given their ability to probe nanostructural (1–200 nm) fluid features that are relevant for the majority of complex fluids. To circumvent many of the issues with the mechanical four-roll mill, a fluidic four-roll mill (FFoRM) was proposed by Lee *et al.*, where the control of near-2D flow fields is accomplished by tuning pressure-driven fluid flow in a specially designed geometry [17]. The FFoRM design was recently implemented for use in small-angle neutron scattering measurements by Corona *et al.*; however, due to the large beam sizes and relatively long measurement times required by this technique, only studies of the fluid nanostructure in near-steady-state conditions near the stagnation point were accessible [18].

This lack of abilities to measure fluid microstructures under time-varying flows greatly limits the flow histories that may be probed. To probe time-varying flow histories, one could temporally change the flow fields produced at the stagnation point of the device to simulate arbitrary processing histories, as can be achieved in mechanical four-roll mills [19]. However, the slow response of syringe pumps compared to the mechanical driving of boundaries limits one's ability to rapidly change the flows rendering control of time-varying flows infeasible for studying most complex fluids. Alternatively, one could probe the response of complex fluids to a wide range of deformation histories by probing the nanostructure in the vicinity of the stagnation point in a steady flow

field, where the nanostructure of the fluid is dependent on the Lagrangian flow history of a material element as it moves along a streamline in the flow. By correlating such Lagrangian flow histories to measurements of fluid structure along them, one can thus produce processing-structure datasets under a more diverse range of flow histories. Importantly, the spatial resolution within the flow field dictates the temporal resolution of the fluid structure along a Lagrangian trajectory in such measurements. Therefore, this alternative approach requires measurement techniques that can resolve nanostructural fluid features with very fine spatial resolution.

An ideal technique for probing fluid nanostructure with fine spatial resolution is *in situ* scanning small-angle x-ray scattering (sSAXS), which has been previously demonstrated for probing the nanostructure of complex fluids in their native flowing environment [20]. The sSAXS technique using synchrotron radiation enables one to create a two-dimensional spatially resolved map (in this work, with 25- μm resolution) of the quantitative variation of nanostructural features (1–200 nm) in a region of interest. This technique can be applied to any complex fluid with sufficient contrast for x-ray scattering to obtain the dependence of, for example, nanostructure shape, conformation, alignment, and size on the flow history the fluid has experienced [20–24]. Thus, the technique can be used as an imaging technique, as well as to collect spatially resolved structural information. So far, *in situ* sSAXS measurements in flow have been limited to geometries that produce specific deformation histories, e.g., contraction/expansion geometries [25,26]. However, a complete fingerprinting of the fluid's response requires measurement capabilities that rapidly probe a much wider range of flow histories comparable with those that are experienced in applications. Therefore, the implementation of the FFoRM geometry into sSAXS instrumentation represents a unique means for probing complex fluid nanostructure under a wide range of flow histories. In this work, we report the measurements of complex fluids with the FFoRM geometry incorporated into sSAXS instrumentation. As a model test material, the study employs dispersions of rodlike nanoparticles dispersed in a Newtonian suspending fluid. Rodlike nanoparticle dispersions are ideal systems for these studies for two reasons: the flow-induced orientation of the nanoparticles produces a strong and easily interpreted signature in the scattering, and dispersions of rodlike nanoparticles are one of the few complex fluids where a micromechanical model exists [27–30]. The relevant theory will be outlined in detail later in this work but, importantly, it assumes completely rigid particles interacting through hard rod interactions. Therefore, probing the roles of flexibility and particle-particle interactions produces important experimental insight into how this theory may be extended to account for flexible particles and more complicated interaction potentials. For this study, we formulate two dispersions of rodlike nanoparticles: one with more rigid cellulose nanocrystals (CNCs) and one with more flexible cellulose nanofibrils (CNFs). Given the strong scattering signature and the ability to compare to micromechanical theories, the measurements reported here will offer an ideal starting point to begin data-driven model formulation with the possibility for comparisons to theory.

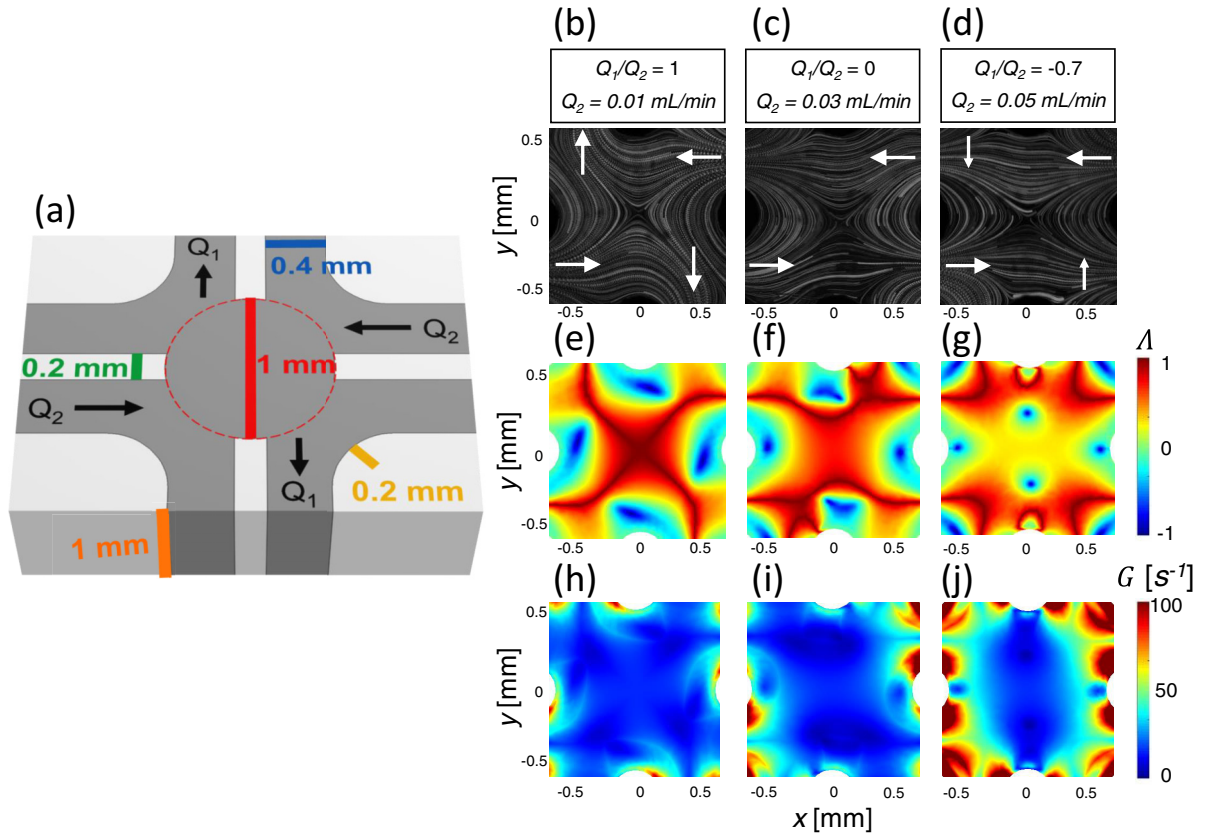


FIG. 1. Description of the FFoRM operation. (a) FFoRM 3D geometry dimensions for sSAXS sample environment adapted from Corona *et al.* [18]. (b)–(d) Streakline images. (e)–(g) Flow-type mapping and (h)–(j) deformation rate-mapping for flows within FFoRM geometry across the device midplane at various conditions corresponding to Q_1/Q_2 of (b), (e), (h) 1; (c), (f), (i) 0; and (d), (g), (j) -0.7 producing flows near the stagnation point ($x = y = 0$) with flow types of (b) 1, (c) 0.8, and (d) 0.2. The included streakline images and simulations are for Q_2 of (b), (e), (h) 0.01; (c), (f), (i) 0.03; and (d), (g), (j) 0.05 mL/min, which produce flows near the stagnation point with $G \sim 10 \text{ s}^{-1}$.

In this work, we begin by outlining the validation procedure for sSAXS in the FFoRM including how measurements are made that correspond to a wide range of flow histories and the formulation of the test fluids. We follow by presenting the results of the sSAXS measurements in the FFoRM for the CNC dispersions and track the structural evolution of the dispersion through representative Lagrangian flow histories to provide a sample of the substantial datasets that can be acquired. Next, we include measurements of the CNF dispersion to demonstrate how the information obtained by sSAXS in the FFoRM varies with the details of the material probed. Lastly, we introduce an analysis method whereby the effect of interparticle interactions on the structure of rigid rodlike dispersions may be isolated from the effects of particle alignment, enabling a comparison between the flow-induced structure of rodlike dispersions with varying interparticle interactions under nearly arbitrary flow histories.

II. METHODS

A. sSAXS in the FFoRM

The fluidic four-roll mill is a device capable of producing arbitrary, near-2D steady-state or time-varying flows of complex fluids [Fig. 1(a)] near a stagnation point in the center of

the device [17,18]. A summary of the device modifications to enable sSAXS measurements in the FFoRM are included in the Experimental Methods section. The inset of Fig. 1 includes a schematic of the FFoRM geometry. The device consists of eight channels that feed into a circular area in the center of the device. By controlling the flow rates in four of these channels (where two channels are held at some flow rate Q_1 and the other two channels are held at a different flow rate Q_2) and holding the remaining channels at constant (ambient) pressure, one can tune the flow fields that are produced in the device. The discussion on the operation of the device will focus on the flows produced near the stagnation point of the device, although changing the flow rates in the inlet/outlet channels will completely alter the full flow fields.

The type of flow encountered by a complex fluid in the FFoRM is determined by the local (spatially varying) velocity gradient tensor ($\nabla \mathbf{u}$). For the remainder of this work, we assume that the velocity field in the FFoRM device is quasi-2D because components of the velocity gradient tensor in the out-of-plane direction are much smaller than those in-plane (see Corona *et al.*) [18]. In general, local 2D velocity gradients can be parametrized by two parameters and a direction. In this work, we choose to parametrize the flow using a flow-type parameter (Λ) and a deformation rate (G) and we choose the direction to be coincident with the principal strain-rate axis

[31]. The flow-type parameter is defined as

$$\Lambda = \frac{|\mathbf{E}| - |\mathbf{\Omega}|}{|\mathbf{E}| + |\mathbf{\Omega}|}, \quad (1)$$

where \mathbf{E} is the rate of strain tensor ($\mathbf{E} = [\nabla\mathbf{u} + \nabla\mathbf{u}^T]/2$), $\mathbf{\Omega}$ is the vorticity tensor ($\mathbf{\Omega} = [\nabla\mathbf{u} - \nabla\mathbf{u}^T]/2$), and $|\mathbf{A}| = \mathbf{A} : \mathbf{A}^T$. The flow-type parameter describes the relative influence of elongation (or strain) compared to rotation (or vorticity). The deformation rate is defined as $G = |\nabla\mathbf{u}|/\sqrt{1 + \Lambda^2}$ and describes the strength of the applied deformation field. G is equal to the shear rate, $\dot{\gamma}$, in simple shear flow (i.e., $\Lambda = 0$) and G is equal to the extension rate, $\dot{\epsilon}$, in an extensional flow (i.e., $\Lambda = 1$). With this parametrization, the local velocity gradient tensor with axes coincident with the principal rate-of-strain axes can be written as

$$\nabla\mathbf{u} = \frac{G}{2} \begin{bmatrix} 1 + \Lambda & 1 - \Lambda & 0 \\ -(1 - \Lambda) & -(1 + \Lambda) & 0 \\ 0 & 0 & 0 \end{bmatrix}. \quad (2)$$

The FFoRM geometry offers the ability to independently tune Λ and G near the central stagnation point of the device by varying Q_1/Q_2 and $Q_1 + Q_2$, respectively (see Fig. 1). For example, a condition where $Q_1/Q_2 = 1$ produces a planar extensional flow ($\Lambda = 1$) near the stagnation point with an extension rate proportional to $Q_1 + Q_2$. More information on controlling flows in the FFoRM can be found in previous work [18], and for the remainder of this work, we will only report flow fields with respect to the values of Λ and G produced near the stagnation point as determined by computational fluid dynamics (CFD) simulations of a Carreau fluid and confirmed with particle-tracking velocimetry (PTV) measurements.

sSAXS measurements enable one to probe nanostructural features within a material (Fig. 2). The scattering of x rays from a material is measured at some angle defined by the scattering vector $\mathbf{q} = (4\pi/\lambda) \sin(\theta/2)$, where λ is the wavelength of the x-ray beam and θ is the angle between the incident beam and the scattering direction. The intensity of scattered x rays is proportional to the Fourier transform of scattering density correlations within the material and is typically expressed as

$$\overline{I(\mathbf{q})} = c \overline{P(\mathbf{q})S(\mathbf{q})}, \quad (3)$$

where $I(\mathbf{q})$ is the measured scattering intensity, $P(\mathbf{q})$ is the form factor, $S(\mathbf{q})$ is the structure factor, c is a constant dependent on the material composition and concentration, and the overbar represents an ensemble average of the quantity. This expression assumes that the particles are of uniform scattering length density, the fluid is incompressible, and that the measured scattering is free from multiple scattering events. We highlight that since the ensemble averaging occurs over the product of the form factor and structure factor, this factorization requires no further assumptions [32]. The form factor includes scattering contributions due to intraparticle correlations (i.e., scattering density correlations within a single particle) while the structure factor includes scattering contributions due to interparticle correlations (i.e., scattering density correlations between particle centers of mass). At the particle concentrations considered in this work, contributions to the scattering from the form factor dominate at high- q values while contributions from both the form factor

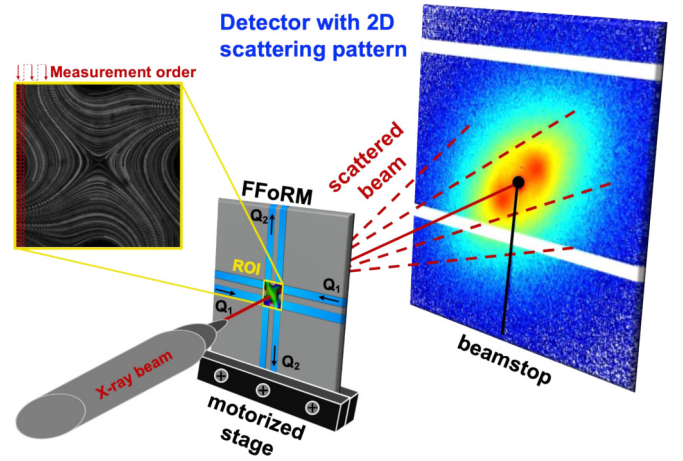


FIG. 2. Overview of sSAXS in the FFoRM methodology. A small coherent x-ray beam is rastered throughout the region of interest (ROI). The FFoRM geometry was implemented at a synchrotron beamline, which offers the ability to collect spatially resolved SAXS patterns. The collected 2D SAXS patterns (right) resolve nanostructural (~ 1 – 200 nm) features in the system with ~ 25 – μm spatial resolution indicated by the red circles on the flow-field image. The flow fields produced in the FFoRM can be manipulated by changing the flow rates into the device (Q_1 and Q_2). The blowup of the ROI shows PTV measurements of a generated elongational flow field.

and structure factor must be considered at low- q values. The transition between the high- q and low- q regimes is related to the average particle separation distance, d , as $q \sim 2\pi/d$, where q is the magnitude of the scattering vector. For the CNC and CNF dispersions, $d \sim 40$ nm, estimated from the point where the measured scattering deviates from the form factor (see Supplemental Material, Fig. B1) [33]. In this work, we are primarily interested in the anisotropy of scattering density correlations within the material, as these provide information about the alignment and spatial positioning of particles in the high- q and low- q regimes, respectively.

The orientation analysis is described in detail in Ref. [34]. In brief, SAXS data were reduced by azimuthal integration to 16 azimuthal segments. The azimuthal distribution of the integrated intensities is well approximated by a sine function (see Supplemental Material, Fig. C1) [33].

$$I(n_\phi, q_{\min} < q < q_{\max}) \approx a_0(q_{\min}, q_{\max}) + a_1(q_{\min}, q_{\max}) \times \sin\left(\frac{2\pi n_\phi}{N_\phi} - \phi_0(q_{\min}, q_{\max})\right), \quad (4)$$

where n_ϕ is the index corresponding to a particular azimuthal interval, N_ϕ is the total number of azimuthal intervals, and the integration interval along q is between q_{\min} and q_{\max} . The baseline $a_0(q_{\min}, q_{\max})$ is the average scattering within the integration range, whereas the amplitude $a_1(q_{\min}, q_{\max})$ is given by its oriented part, i.e., its anisotropic component. The degree of scattering anisotropy can be parametrized by $\alpha(q_{\min}, q_{\max}) = a_1(q_{\min}, q_{\max})/a_0(q_{\min}, q_{\max})$, which compares the amplitude of scattering anisotropy to the average magnitude of scattering intensity. This degree of anisotropy is assumed to be correlated to the degree of particle alignment

in the fluid [35]. The phase shift of the sine function, ϕ_0 , represents the azimuthal angle at which the scattering intensity has a minimum. Since the scattering intensity is proportional to the Fourier transform of scattering density correlations in the material, it also represents the direction of maximum density correlations, i.e., the most probable direction of particle orientation. In other words, the maximum scattering intensity is perpendicular to the particle alignment direction. These parameters are quickly extracted from a discrete Fourier transform of the integrated intensities.

In this work, we chose two distinct q ranges, a high- q regime ($0.030\text{--}0.050\text{ \AA}^{-1}$, $qd/2\pi \sim 1.9\text{--}3.2$) and a low- q regime ($0.010\text{--}0.014\text{ \AA}^{-1}$, $qd/2\pi \sim 0.64\text{--}0.89$), corresponding to the intraparticle scattering regime [i.e., the form factor, $P(\mathbf{q})$] and the interparticle scattering regime [i.e., the structure factor, $S(\mathbf{q})$], respectively. We define the high- q and low- q degree of scattering anisotropy as $\alpha_{\text{high-}q} = \alpha(0.03\text{ \AA}^{-1}, 0.05\text{ \AA}^{-1})$ and $\alpha_{\text{low-}q} = \alpha(0.01\text{ \AA}^{-1}, 0.014\text{ \AA}^{-1})$, respectively. For a single SAXS measurement, differences between $\alpha_{\text{high-}q}$ and $\alpha_{\text{low-}q}$ will be driven by differences in $S(\mathbf{q})$. In the limit as $q \rightarrow 0$, the deviation of $S(\mathbf{q})$ from unity is inversely proportional to the second virial coefficient, B_2 , which parametrizes the strength of interactions between rods [36]. When attractive interactions dominate, $B_2 < 0$, $S(\mathbf{q})$ increases at low- q -values, and therefore $\alpha_{\text{high-}q} < \alpha_{\text{low-}q}$. When repulsive interactions dominate, $B_2 > 0$, $S(\mathbf{q})$ decreases at low q -values and therefore $\alpha_{\text{high-}q} > \alpha_{\text{low-}q}$. This relationship between particle-particle interactions and relative degree of alignment in different q ranges will be further discussed when presenting the experimental results.

B. Test fluid formulation

To test the capabilities of sSAXS in the FForM, we formulated two dispersions of rodlike nanoparticles: cellulose nanocrystals (CNCs), which are shorter and stiffer nanoparticles ($\langle L \rangle \sim 150\text{ nm}$ and $\langle L \rangle/l_p < 0.2$) where $\langle L \rangle$ is the average particle length and l_p is the persistence length), and cellulose nanofibers (CNFs), which are longer and more flexible ($\langle L \rangle \sim 500\text{ nm}$, $\langle L \rangle/l_p \sim 0.2$), although both particles are considered rigid in the sense that $\langle L \rangle/l_p < 1$ [37]. We chose these test fluids due to the strong scattering signature for the alignment of the particles and the ability to compare results to microscopic models for rigid rods. The microscopic model that we will be testing in this work is the modified Dhont-Briels model, which includes an effective external mean-field potential to account for hard rod interactions with other particles [29,30]. The important parameters in this theory are the rotational diffusivity D_r , which describes the effect of thermal fluctuations on the orientation of the particles and the effective particle concentration $L\phi/d$, where ϕ is the particle volume fraction, L is the particle length, and d is the particle diameter. The rotational diffusivity for dilute, finite-length, high aspect ratio, cylindrically shaped particles can be calculated as

$$D_{r,0} = \frac{3k_B T}{\pi \eta_s L^3} \left(\frac{1 - \frac{1.5}{\ln(2L/d)}}{1 + \frac{0.64}{\ln(2L/d)}} \right), \quad (5)$$

where $k_B T$ is the thermal energy and η_s is the solvent viscosity. To account for the effect of particle interactions on the

rotational diffusivity, Doi *et al.* proposed that the zero-shear rotational diffusivity may be expressed as

$$D_r = \beta D_{r,0} [4\phi(L/d)^2]^{-2}, \quad (6)$$

where $\beta = 1.3 \times 10^3$ is a constant prefactor determined from Brownian dynamics simulations and ϕ is the volume fraction of rods [38–40]. The modified Dhont-Briels model interpolates between the zero-shear diffusivity for rods that are oriented isotropically and the dilute particle diffusivity when the rods are highly aligned. From a physical perspective, the model includes interparticle interactions at low shear rates leading to an effectively slowed diffusivity; but, the effect of interactions vanishes as the rods become aligned, thus increasing the rotational diffusivity to the dilute case.

The test fluids for these studies include a 4 wt % dispersion of CNCs in a mixture of water and glycerol and a 0.25 wt % dispersion of CNFs in water. The concentrations were chosen such that $L\phi/d \approx 0.5$. As such, in both dispersions the strength of excluded volume particle interactions as predicted by the modified Dhont-Briels model are equal. To correct for differences in rotational diffusivity, the solvent composition was chosen such that D_r is approximately equal to 2 s^{-1} for both dispersions. This was accomplished through the addition of glycerol, a viscous ($\eta_s \approx 1\text{ Pa s}$) water-soluble solvent, to the CNC dispersion. By formulating the samples in this way, we intended to isolate the effects of particle flexibility, aspect ratio, and interactions on the flow behavior of rod-like nanoparticle dispersions in a way that is independent of the rod concentration and rotational diffusivity. Tuning D_r is especially important because the alignment of rods in dilute dispersions is dictated by a dimensionless group, the rotational Péclet number ($Pe_r = G/D_r$).

Regarding particle-particle interactions beyond excluded volume, CNCs have been found to interact repulsively due to electric double-layer interactions between the particles associated with their surface charge [41]. The characterization of repulsive interactions between CNC particles is supported by equilibrium SAXS measurements of the formulated CNC dispersion, where the measured scattering intensity is less than the predicted scattering accounting only for the form factor (see Supplemental Material, Fig. B1) [33]. Similar repulsive interactions are expected for dispersions of CNFs, as supported by zeta-potential measurements and the impact of adding salt on particle aggregation behavior [23,42]. However, we find the formulated CNF dispersion has a measured equilibrium scattering intensity that is higher than the predicted form factor scattering, suggesting attraction-driven aggregation (see Supplemental Material, Fig. B1) [33]. A Derjaguin-Landua-Verwey-Overbeek (DLVO) model for the interaction potential between CNFs predicts repulsive potentials for crossed rods on the order of thermal energy (kT), whereas the model for CNCs predicts these potentials are on the order of 10 kT for a 1:1 electrolyte concentration on the order of 10 mM [41,43]. Comparing these models suggests that aggregation and a more positive value of the second virial coefficient is to be expected in the CNF dispersion, which is consistent with the observed small levels of aggregation in the measured equilibrium scattering. As a result of this difference, comparative measurements between these two systems may offer physical insight into the effects of differences in particle-

particle interactions on the flow-induced structure of rodlike dispersions.

Many studies have probed the nanostructure of cellulose-derived nanoparticles in certain flow types, but as we will demonstrate in this work, sSAXS measurements in the complex flow fields produced by the FFoRM provide insight into the response of nanostructure to a wide range of Lagrangian deformation histories, e.g., transient and inhomogeneous flows. Lagrangian trajectories were chosen near the center plane of the geometry, as this region generates the largest in-plane velocity gradients. In reality, SAXS measurements probe the structure through the full thickness of the device where the velocity gradients vary in G (but not Λ) [18]. For this work, we neglect this variation in G and report values corresponding to the center plane of the geometry. To determine these Lagrangian trajectories, we utilize 3D CFD simulations in COMSOL of a Generalized Newtonian fluid with a viscosity described by a Carreau model fit to measured shear rheology (see Supplemental Material [33]). CFD simulations were used to enable higher spatial (and therefore temporal) resolution toward the calculation of the flow histories than are currently accessible with PTV measurements. In this work, we will only include results from Lagrangian trajectory mapping by CFD and confirmed by PTV for the CNC dispersion, which was found to be weakly shear thinning (see Supplemental Material [33]). It was found in Corona *et al.* that the flow fields for weakly shear thinning fluids in the FFoRM could be predicted with such simulations [18]. Upon determining the velocity fields for the range of experimentally probed conditions, the velocities and velocity gradients for various streaklines were determined numerically. Along each trajectory, we calculate the accumulated strain at a certain point x_n as

$$\gamma(x_n) = \int |\mathbf{E}| dt = \int_{x_0}^{x_n} |\mathbf{E}|(x) \frac{dx}{U(x)} \approx \sum_{x=x_0}^{x_n} |\mathbf{E}|(x) \frac{\Delta x(x)}{U(x)}, \quad (7)$$

where $U(x)$ is the velocity at position x , Δx is the distance between the point of interest and the previous point, x_0 is the point where we begin tracking accumulated strain, and $|\mathbf{E}|$ is the magnitude of the rate of strain tensor. The integral is evaluated along the streamline, which implicitly assumes that the macroscopic flow field is steady over time in the Eulerian reference frame, and is confirmed by PTV measurements of the flow fields. Additionally, we calculate Λ , G , and the accumulated strain from the CFD simulations. For brevity, we do not report the direction of the principal straining axis in this work, although this may also be quantitatively extracted from these simulations. Qualitatively, the principal straining axis points in the outflow direction near the stagnation point and perpendicular to the streamlines in the direction of the flow in the inlet/outlet flow regions. With this Lagrangian trajectory mapping, we can correlate the deformation history of a fluid element with structural measurements determined with sSAXS.

III. RESULTS

A. Lagrangian mapping of soft material order

The combination of sSAXS measurements, CFD simulations, and PTV enables one to probe the impact of an imposed

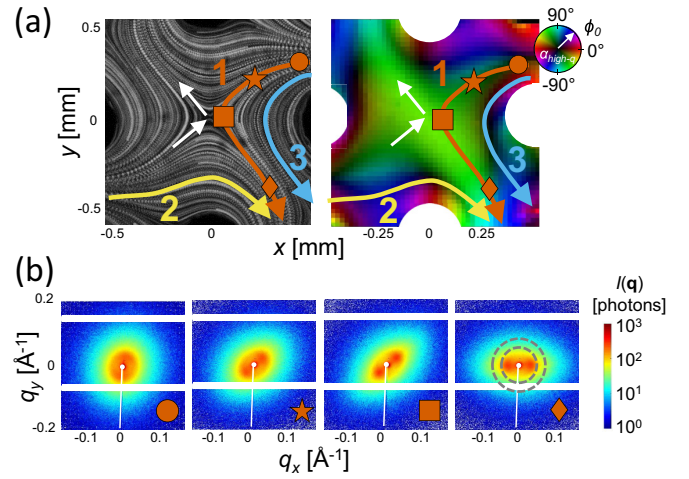


FIG. 3. Lagrangian mapping of flow histories and their corresponding nanostructure evolution using sSAXS. (a) Streaklines and alignment mapping for a 4 wt % CNC dispersion in the FFoRM geometry under conditions corresponding to an extensional flow where the white arrows indicate the direction of the flow. The streakline trajectories (colored arrows) are long-exposure images of non-Brownian tracers in the fluid. The alignment mapping provides the direction (ϕ_0) and degree of alignment ($\alpha_{\text{high-}q}$) as measured with sSAXS. The hue indicates the direction of alignment of the particle and the intensity of the point indicates the degree of alignment, where lighter points correspond to a higher degree of alignment, as indicated by the color wheel in the top right. (b) Representative SAXS patterns at three different points along the Lagrangian trajectory 1 (orange) indicated by the colored symbols circle, star, square, and diamond in (a). The gray dotted lines in the rightmost pattern in (b) indicate the edges of the q range used in the annular averaging to extract ϕ_0 and $\alpha_{\text{high-}q}$ (between 0.03 and 0.05 \AA^{-1}). The white regions in (b) indicate areas of the detector where scattering was not measured either due to presence of the beamstop or the gaps between detector modules.

flow history on the order of a soft material of interest. In a demonstrative example, we explore the ordering of the CNC dispersion in the FFoRM operating such that a flow with $\Lambda \approx 1$ and $G \approx 10 \text{ s}^{-1}$ occurs near the stagnation point. When the deformation field within the FFoRM is known, either via PTV measurements and/or CFD simulations, one can translate the spatially resolved sSAXS measurements into emulated SAXS measurements along Lagrangian deformation histories (Fig. 3). For illustrative purposes, three representative trajectories were chosen from streakline images captured via PTV and superimposed on the sSAXS spatial mapping [Fig. 3(a)]. This superposition enables us to map measured SAXS patterns to various points along Lagrangian streamlines [Fig. 3(b)]. This enables direct inference of the structural response of the fluid to a transient flow involving time variations in flow type and strain rate. For example, following the example trajectory 1, we find that the CNC dispersion is completely disordered as it enters the measurement region [top right of Fig. 4(a, ii)] and gradually becomes ordered as it approaches the stagnation point, as indicated by the increased degree of scattering anisotropy. After its approach toward the stagnation point, the CNCs remain ordered as the fluid is

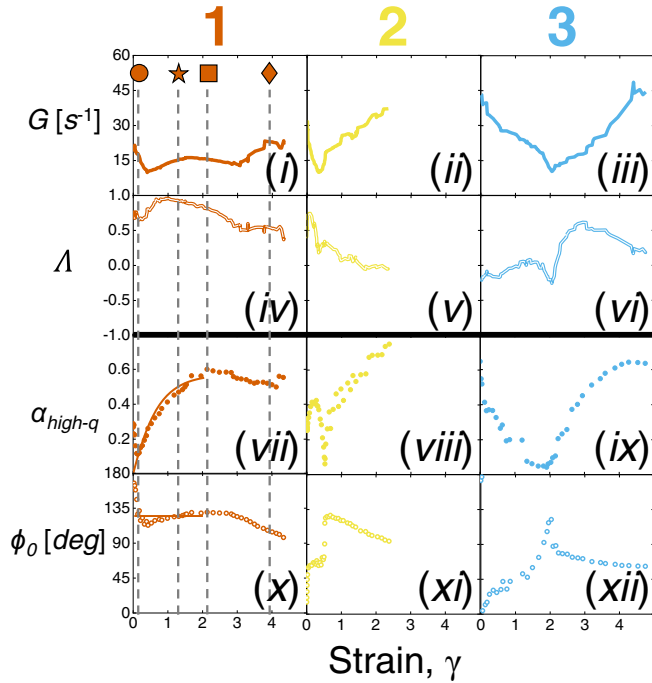


FIG. 4. Lagrangian orientation mapping along representative streamlines. Representative orientation mappings are included for streamlines 1 (orange), 2 (yellow), and 3 (blue) indicated in (Fig. 3). For a given deformation history parametrized by the deformation rate (G) and flow-type parameter (Λ), the measured degree of alignment ($\alpha_{\text{high-}q}$) and alignment direction (ϕ_0) are included as a function of strain ($\gamma = |\mathbf{E}|t$). For Lagrangian trajectory 1, the gray dotted lines indicate the points corresponding to the circle, star, square, and diamond in (a) and (b) and the orange-colored line in the measured α and ϕ_0 (vii and x) includes model predictions for the order parameter from simulations of the modified Dhont-Briels model in the startup of extensional flow with $Pe_r = 5$, $\Lambda = 1$, $L\phi/d = 0.5$.

convected toward the exit channel, resulting in the observed asymmetry in the spatial alignment mapping. Finally, the Lagrangian trajectories can be translated from a spatial map to a strain-dependent history in terms of the deformation histories along the trajectory using CFD simulations (Fig. 4). Here, for expedience, we calculate Λ , G , and the accumulated strain from numerical simulations of flow in the device (for details, see Ref. [18]). The deformation rate (G) and flow type (Λ) are tracked along the three example Lagrangian trajectories as a function of the accumulated strain ($\gamma = |\mathbf{E}|t$) and matched to the resulting structure of the fluid measured with SAXS, given here in terms of the high- q (i.e., intraparticle) degree of alignment ($\alpha_{\text{high-}q}$) and the direction of the alignment (ϕ_0).

In all previously reported flow-SAS experiments, measurements of the fluid structure are analyzed such that the flow the material experiences is assumed to be a single, time-invariant flow type (Λ). For example, rheo-SANS devices produce simple shear flows ($\Lambda = 0$), while various fluidic devices have been constructed to probe extensional ($\Lambda = 1$) or complex flows ($0 < \Lambda < 1$) [25,26]. By contrast, with the analysis presented in Figs. 3 and 4, one can directly relate the nanostructural changes of a soft material to the complete flow history the material has encountered to that point, including

time-varying flow types (Λ). Furthermore, the FFoRM produces a wide array of flow histories in a single operating condition. Given that there are 20 measurements resolved across the width of the two inlet channels, one could resolve a minimum of 40 *full* Lagrangian trajectories in a single measurement. One may also consider that the measurement probes the structure at approximately 2000 individual points in the flow correlating with approximately 2000 unique flow histories. The representative cases provided in Figs. 3 and 4, can be coarsely described in terms of familiar processing flows. These flow histories range from a steady extensional flow (trajectory 1, orange), a deformation rate ramp in simple shear flow (trajectory 2, yellow), and a change from simple shear flow to extensional flow (trajectory 3, blue). For the case of trajectory 1, we find that the nanostructure aligns in a single direction along the extensional axis and $\alpha_{\text{high-}q}$ increases monotonically to a plateau value with trajectory 1 plateauing at a higher value. Trajectories 2 and 3 undergo a much different response, where the direction that the nanostructure aligns along changes and results in a decrease followed by an increase in $\alpha_{\text{high-}q}$.

Such measurements can inform our understanding of the impact of flow history on the structure of the fluid of interest. In the case of the CNC dispersion, we compare the experimentally measured $\alpha_{\text{high-}q}$ under the startup of steady extensional flow (Fig. 4vii) to predictions for the order parameter, i.e., the difference between the principal moments of the orientation distribution function, from the modified Dhont-Briels model [30]. We find that the modified Dhont-Briels model predictions in the startup of a steady extensional flow match the initial ($0 < \gamma < 2$) time-dependent ordering of the CNC dispersion along trajectory 1, where the flow history can be approximated as the startup of an extensional flow ($Pe_r = 5$, $\Lambda = 1$). In conventional flow-SAS measurements, analysis has been limited to trajectories where the flow is approximately homogeneous in flow type and deformation rate. As highlighted in this example, such regions represent a limited portion of a single flow trajectory. With sSAXS measurements in the FFoRM, one can access the full range of many such trajectories. Furthermore, this example demonstrates that sSAXS in the FFoRM provides the opportunity to test rheological models under complete, complex flow histories rather than only those in idealized rheometric flows. Model comparisons under the experimentally realized complex flow histories will be the subject of future work. Overall, the sSAXS measurements in the FFoRM confirm that the development of order in the CNC dispersion depends on the entirety of the fluid's flow history rather than simply the local deformation field, proving the need for mapping the fluid's full Lagrangian flow history.

B. Variation of flow fields and flow histories

The previous analysis focused on the operation of the FFoRM with one set of inlet/outlet flow rates. However, the FFoRM is designed such that these flow rates can be varied to produce nearly arbitrary 2D flows near the stagnation point, where the material with the longest steady-state accumulated strain is located. Therefore, by changing the inlet/outlet flow rates, one changes the flow histories that are probed in a sSAXS measurement. To probe the nonequilibrium

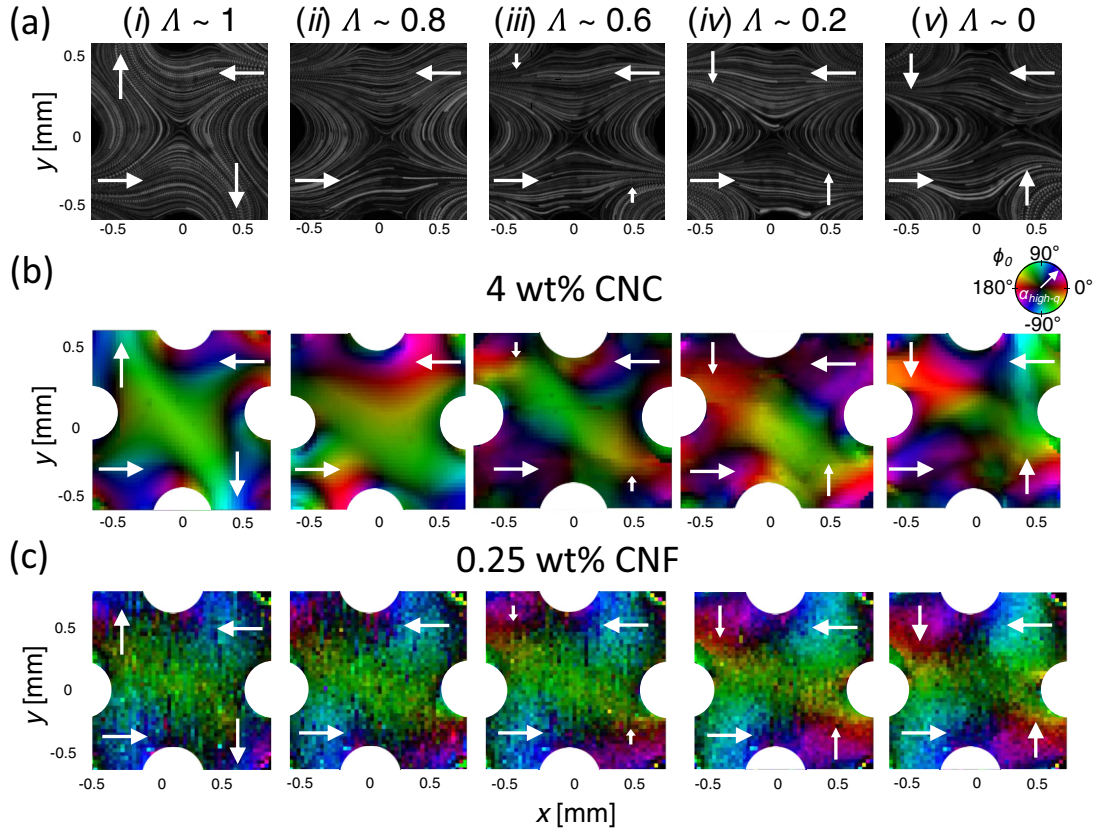


FIG. 5. Alignment mapping with varying flow conditions. (a) Streakline images for flows in the FForM at five conditions corresponding to Λ of (i) 1, (ii) 0.8, (iii) 0.6, (iv) 0.2, and (v) 0 near the stagnation point. The white arrows indicate the direction and magnitude of the flow from the inlet channels while the length of the arrow is proportional to the magnitude of the flow rate. SAXS alignment mapping of the (b) 4 wt % CNC dispersion and (c) 0.25 wt % CNF dispersion for the inlet conditions corresponding to the streaklines above in (a). The hue of each point indicates the direction of alignment of the particles as indicated by the color wheel in the top left and the intensity indicates the a_1/a_0 where lighter points correspond to a higher α . The values were calculated in the intraparticle regime (between $q = 0.03$ and 0.05 \AA^{-1}).

nanostructure of the CNC dispersion under a wider range of flow histories, we vary the inlet conditions such that the flow fields produced near the stagnation point vary from the previously analyzed extensional flow ($\Lambda \approx 1$) to simple shear flow ($\Lambda \approx 0$) and the deformation rate, G , is held approximately constant at 10 s^{-1} [Fig. 5(b)]. For the flow rates into and out of the device indicated by the white arrows, we report the streaklines for the flows produced as measured with PTV [Fig. 5(a)] and the spatially mapped order as measured with sSAXS [Fig. 5(b)].

For all five flow conditions, we find that the alignment of the microstructure near the central stagnation point is approximately in the same direction at -45° (or equivalently 135°), which corresponds to the principal strain-rate axis and is nearly constant in the FForM geometry for all the inlet/outlet conditions tested. The CNCs align along the principal strain-rate axis for deformation rates of 10 s^{-1} and flow types ranging from extensional to simple shear flow in agreement with the previous study [18]. We also find that the CNC dispersion always has a lower degree of alignment while approaching the stagnation point than when it has already passed near the stagnation point. This discrepancy between material approaching and leaving the stagnation point is a result of the history-dependent alignment of the CNC, which appears regardless of the applied flow type and arises due

to the nonlinear coupling of orientation and viscoelastic dynamics of the fluid. By changing the flow near the stagnation point of the device, we produce flow histories that correspond to a startup flow from an initially relaxed configuration, e.g., from material that enters near the center of the inlet channel, similar to trajectory 1 in Fig. 3, and so these measurements provide information about how different flow types affect the structure of soft materials under the startup of complex flows. Conversely, some of the Lagrangian trajectories have not relaxed from their entry flow history, e.g., trajectories entering the measurement region near the channel walls, similar to trajectory 3 in Fig. 3. These trajectories are indicative of the structural response under a flow that varies from simple shear flow to the flow of interest. By probing trajectories that enter the measurement region closer to or further from the channel walls, one can examine the effect of different initial starting structures ranging from those under a steady simple shear flow to those in an isotropic configuration. Another notable difference occurs as the flows near the stagnation point approach simple shear flow (i.e., Λ closer to 0), where we find that the alignment maps are no longer symmetric with respect to the outflow axes. This broken symmetry occurs because the flow fields produced are similarly not symmetric because the stagnation point moves from its expected location near the center of the FForM geometry [e.g., Fig. 5(a), v].

Despite this, as long as the flow is steady and reproducible, PTV measurements can provide the required local velocity and velocity gradient fields necessary for Lagrangian flow mapping.

We now consider the amount of structural information collected from sSAXS measurements in the FFoRM. Previously, we noted that a measurement taken at a single condition yielded approximately 2000 measurements at different times in the fluid's flow history. For just the CNC sample, we probed combinatorial conditions corresponding to five values of Λ and 8 values of G , resulting in nanostructural measurements under approximately 80 000 unique flow histories. Furthermore, the measurement time per condition was approximately 15 min, including the time for the flow to reach steady state, meaning that these measurements were completed in 10 h. Therefore, sSAXS in the FFoRM appears to present the capabilities necessary for data-driven rheological modeling approaches. Since such data-driven approaches are not yet prevalent, in their present form these datasets offer insight into the flow-induced structure of rodlike nanoparticle dispersions, which we will now illustrate through a comparison between a CNC and CNF dispersion.

C. Varying fluid interactions and rheology

While to this point we have focused on a single fluid, sSAXS measurements in the FFoRM can be performed with fluids of varying structure and rheology. We investigated the CNF dispersion described previously, which differs from the CNC dispersion in several critical ways: the CNFs are less rigid, longer particles that tend to have less repulsive effective interparticle interactions compared to the CNCs. As mentioned before, we have formulated the two dispersions such that the effective concentration ($L\phi/d$) and rotational diffusivity are nearly equal. Despite these similarities between the samples, the CNF dispersion's rheological response is that of a yield stress fluid compared to the slightly shear thinning response of the CNC dispersion. Previously it was shown that the flows of yield stress fluids are well behaved in the FFoRM geometry and similar to those of a Newtonian fluid; therefore, we do not report PTV streaklines for this dispersion as they are similar to those presented in Fig. 5(a) [18]. Furthermore, we do not include the full Lagrangian flow mapping for the CNFs as we will focus on a qualitative comparison between the samples for this first study. The alignment mapping of the CNF dispersion under the same conditions as the CNC dispersion is shown in Fig. 5(c).

Similar to the CNC dispersion, we find that the direction of alignment near the stagnation point is in the direction of the principal strain-rate axis, and the degree of alignment is higher for larger Λ . We also find that the direction of alignment of CNFs in the regions away from the stagnation point is very similar to those from the alignment mapping of the CNCs, suggesting that both the flow fields produced by the fluids and the coupling of the particle alignment to the flow field are very similar in these regions. Unlike the CNC dispersion, the scans reveal regions of weak alignment and regions of strong alignment in similar areas of the scan, e.g., Fig. 5(c) displays sharper spatial variation in $\alpha_{\text{high-}q}$ than Fig. 5(b). Since the flows remain at steady state, this variability in the

structure at similar regions in the flow is likely a result of inhomogeneities in the fluid, i.e., the fluid has local regions where the nanostructure can align in the flow and others where alignment does not occur. Besides the change in $\alpha_{\text{high-}q}$, there is a small intensity increase in the scattering intensity. We do not fully understand this result at this time, but we propose two possible explanations. The analysis presented in Fig. 5 was conducted on scattering that is mainly sensitive to intraparticle correlations (i.e., the form factor); thus, the differences in the $\alpha_{\text{high-}q}$ values are not directly resulting from aggregation or local differences in particle-particle interactions between CNFs. However, interparticle interactions between the CNFs can also modify the distribution of particle orientations. Therefore, local changes in interparticle interactions may be affecting the intraparticle orientation distribution producing the observed sharp changes in the particle alignment. An alternative explanation is that the density of CNF fibers is inhomogeneous due to particle aggregation, for example. In this situation, while the interaction potential between fibers remains unchanged, local increases and decreases in particle concentration have a significant effect on the particle alignment in the same way as macroscopic changes in concentration effect particle alignment. A compounding complication is the unknown impact of particle flexibility on local variations in particle interactions and density. It is possible that the flexibility of the CNFs contributes to local variations in interparticle interactions or increases the possibility of particle aggregation.

Another feature of the CNF alignment mapping compared to the CNC is the lack of history dependence in the alignment of the nanostructure. For the CNC dispersion, we found a clear difference between material moving from the inlet toward the stagnation point compared to material moving from the stagnation point toward the outlet. For the CNF dispersion, we find very little difference between these two trajectories, suggesting that the CNFs require a very small amount of accumulated strain to align in a flow field. Overall, we find that the flow-induced structure of the CNF dispersion is noticeably different than that of the CNCs, which we propose is a result of the differences in interparticle interactions, aggregation behavior, particle flexibility, or some combination of these phenomena.

D. Assessing the influence of interparticle interactions on flow-induced order

The previous analyses focused on the interpretation of the intraparticle alignment of the CNC and CNF particles in the high- q value regime of the SAXS data. However, SAXS measurements probe the full range of the material nanostructure, enabling one to resolve other larger-scale structural features of the material, including interparticle correlations [i.e., the structure factor, $S(\mathbf{q})$]. The results in Figs. 5(b) and 5(c) represent 10 000 SAXS patterns, rendering complete model fitting of the \mathbf{q} -dependent scattering computationally challenging. Instead, we turn to a model-free analysis whereby we probe the degree of alignment [$\alpha(q_{\min}, q_{\max})$] at two different length scales (q values) corresponding to the intraparticle structure, i.e., the form factor, and the interparticle (collective) structure, i.e., the structure factor (see the inset of Fig. 6). The value of α at relatively high- q values compared to the

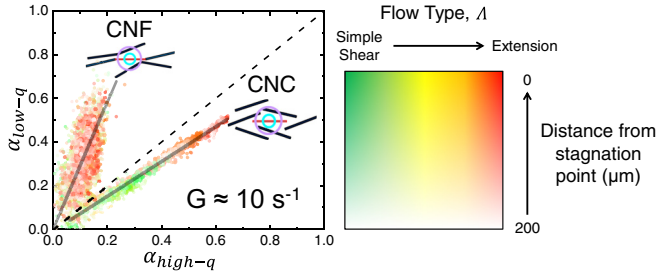


FIG. 6. Nonequilibrium structural comparison between CNC (lower trend) and CNF (upper trend) dispersions. The degree of alignment (α) calculated in two different q ranges corresponding to a high- q (x axis) and low- q (y axis) range and at varying flow conditions (hue and saturation of points) in a 0.2-mm-diameter region centered at $x = y = 0$. The included points correspond to flow conditions where $G \approx 10 \text{ s}^{-1}$ and the flow type varies from $\Lambda \approx 0$ (simple shear flow, green) to $\Lambda \approx 1$ (extensional flow, red) given by the hue of the point while the color saturation of the point indicates the distance the measurement was made from the center of the device as indicated by the 2D color bar on the right. The gray lines are linear fits to the CNC and CNF measurements with slopes of 0.8 and 2.9, respectively, and the black dotted line indicates $\alpha_{\text{high-}q} = \alpha_{\text{low-}q}$. Inset: Pictorial representation of the interpretation of the nonequilibrium structure of the CNF and CNC dispersions under all included flow conditions for equivalent $\alpha_{\text{high-}q}$. Qualitatively, $\alpha_{\text{high-}q}$ is sensitive to the anisotropy of density correlations within the light blue circle while $\alpha_{\text{low-}q}$ is sensitive to the anisotropy of density correlations within the light purple circle.

inverse of the average particle separation length, d , ($q > 2\pi/d$) provides information about the intraparticle alignment of CNC and CNF particles, and is the value that was reported in the previous analysis. By contrast, the value of α at relatively low- q values ($q < 2\pi/d$) depends on contributions from both the alignment of individual particles as well as the spatial distribution of neighboring particles. In general, the value of $\alpha_{\text{low-}q}$ and $\alpha_{\text{high-}q}$ will be approximately equal in a dispersion of dilute particles where interparticle interactions, i.e., $S(\mathbf{q})$, contribute negligibly to the scattering [44]. However, α will be different in the high- q and low- q regimes when interactions between particles are significant because the value of $\alpha_{\text{low-}q}$ is also sensitive to interparticle correlations between particles, i.e., the distribution of center of mass (COM) particle separation distances. If $\alpha_{\text{low-}q} > \alpha_{\text{high-}q}$, this means that there are increased COM correlations with neighboring particles along the direction of alignment, or physically speaking one is more likely to find neighboring particles parallel to the direction of mean particle alignment. Conversely, if $\alpha_{\text{low-}q} < \alpha_{\text{high-}q}$, this means that there are decreased COM correlations with neighboring particles along the direction of alignment, or physically speaking one is less likely to find neighboring particles parallel to the direction of mean particle alignment. This description is consistent with the expected relationship between the virial coefficient B_2 , the anisotropic structure factor $S(\mathbf{q})$, and the relative magnitudes of $\alpha_{\text{low-}q}$ and $\alpha_{\text{high-}q}$ described earlier.

We will now describe how changes in the nature of interparticle interactions may give rise to the previously described changes to COM correlations in aligned particle systems. At low Pe_r , rods adopt both random orientation distributions and

random COM distributions. At high Pe_r , particles become aligned, which produces anisotropic COM distributions that depend on the dominant type of particle interactions. When there are short-range repulsive interactions between particles, the particles will reorganize to minimize contacts with other particles. This results in a decrease in local particle density along the test particle's alignment direction, and therefore $\alpha_{\text{low-}q} > \alpha_{\text{high-}q}$. When there are short-range attractive interactions between particles, the particles will reorganize to maximize contacts with other particles. This results in an increase in local particle density along the test particle's alignment direction, and therefore $\alpha_{\text{low-}q} < \alpha_{\text{high-}q}$. An equivalent way to understand this effect is in terms of the second virial coefficient, B_2 , as described previously. When repulsive interactions dominate: $B_2 > 0$, $S(\mathbf{q} \rightarrow 0) < 1$, and $\alpha_{\text{high-}q} > \alpha_{\text{low-}q}$. When attractive interactions dominate, $B_2 < 0$, $S(\mathbf{q} \rightarrow 0) > 1$, and $\alpha_{\text{high-}q} < \alpha_{\text{low-}q}$.

A representative comparison of $\alpha_{\text{low-}q}$ and $\alpha_{\text{high-}q}$ for the CNC and CNF dispersions (Fig. 6) validates the qualitative picture just described. In particular, we compare measurements on the two materials at similar conditions with a nearly constant deformation rate ($G \approx 10 \text{ s}^{-1}$) and varying flow type (Λ from 0 to 1 as indicated by the color scale). Furthermore, we only include measurements made within 200 μm of the stagnation point, where the flow is nearly homogeneous. Even though the flow is nearly homogeneous, the measurements for a given condition correspond to different points along Lagrangian flow histories, so that points that are further from the stagnation point (signified by the color intensity of the point) tend to have less accumulated strain.

When analyzing the effect of flow history on intraparticle alignment, we find substantial differences between the flow response of the CNCs and CNFs. For the CNCs, the degree of alignment is highly dependent on the flow type and accumulated strain, where the highest degrees of intraparticle alignment are achieved for flows that are more extension dominated (red points) and for material that is closer to the stagnation point where accumulated strains are large (darker points). Conversely, the CNFs show no apparent correlation between flow type or accumulated strain, i.e., the distance from the stagnation point, for a given deformation rate. This observation suggests that while the alignment of CNCs depends on the rate of strain, which is highest for more extension-dominated flows, and the accumulated strain, which is higher for material closer to the stagnation point, the alignment of the CNFs only depends on the deformation rate. To explain this result, we hypothesize that the increased flexibility and changes in interactions between the CNFs restricts the particles' ability to align in a flow field, meaning that higher strain rates are required to produce the strain and strain-rate dependent effects observed in the CNCs. Further supporting this hypothesis, the degree of intraparticle alignment is higher for the CNCs compared to the CNFs for similar flow histories.

When comparing $\alpha_{\text{low-}q}$ and $\alpha_{\text{high-}q}$, we find that the two materials divide into two populations where the ratio $\alpha_{\text{low-}q}/\alpha_{\text{high-}q}$ is nearly constant, but with different values for the two materials. For the CNC dispersion, the interparticle degree of alignment $\alpha_{\text{low-}q}$ is always less than the intraparticle degree of alignment $\alpha_{\text{high-}q}$ (i.e., $\alpha_{\text{low-}q}/\alpha_{\text{high-}q} < 1$), whereas for the CNF dispersion the opposite is the case (i.e.,

$\alpha_{\text{low-}q}/\alpha_{\text{high-}q} > 1$). This is consistent with the expectations outlined previously, in which interparticle repulsions suppress anisotropy of particle COM correlations whereas interparticle attractions enhance it. As such, this suggests that the magnitude of $\alpha_{\text{low-}q}/\alpha_{\text{high-}q}$ relative to unity can be used as a simple, model-free metric for determining whether interparticle attractions or repulsions are more influential with respect to the flow-induced orientational order of the materials probed. Furthermore, the fact that the ratio $\alpha_{\text{low-}q}/\alpha_{\text{high-}q}$ remains constant across all included flow conditions suggests that the interparticle interactions between rods are insensitive to the flow histories probed, even though the collective structure is modified due to the flow-induced orientation of individual particles. Overall, the analysis of the structure of the CNC and CNF dispersions at multiple length scales and under a wide range of flow histories, as afforded by sSAXS in the FFoRM, has revealed that the nature of interactions between rods is unaffected by the flow type at a constant, moderate deformation rate. Furthermore, the dominant characteristic of interparticle interactions (e.g., attraction versus repulsion) is revealed directly by the proposed analysis, without the need for a particular model for describing the anisotropic interactions and the scattering they give rise to.

IV. DISCUSSION

Outlook for surveying complex fluids' response to flow

In the previous example analyses, we have demonstrated the capabilities of the sSAXS in the FFoRM for probing the nanostructure of soft materials under a multitude of unique flow histories. The large datasets made accessible by this technique enable insight into the flow-history dependence of the structure of soft materials. For example, consider the case of fiber spinning, in which one may wish to use flow to align the nanostructure of the material to impart anisotropic mechanical properties. Conventionally, one might design several differently shaped nozzles and measure the nanostructure of the material as it navigates this geometry. Using sSAXS measurements in the FFoRM, one could create a database of the material's response to various flow histories and determine which flow histories are encountered in a particular nozzle design, circumventing the need for making multiple measurements in multiple different nozzles. Such an approach reduces the time spent fabricating devices, aligning samples, and making calibrating measurements because emulating a new nozzle design only requires determining the flow histories that are encountered in the process and creating a relevant FFoRM flow protocol. Additionally, sSAXS in the FFoRM provides an approach to address the inverse problem, i.e., designing a flow geometry to target a desired nanostructure by exploring a rich database of measurements to determine the flow histories that produce the desired nanostructure.

From the perspective of a more fundamental understanding of soft material response to flow, one can use sSAXS measurements in the FFoRM as rigorous tests of physics-based theories or models. Conventionally, comparison to such theories and models are made in simple shear or extensional flows. As a result, there potentially exists a bias in the resulting theories—either in the formulation of the physical models

or in the values of the associated model parameters—toward such “simple” flows that does not reflect the complex coupling between non-Newtonian dynamics and the time evolution of deformation types, such that theories produce inaccurate predictions of flow and structure in more realistic processes. Conversely, sSAXS in the FFoRM enables structural predictions from theories made and compared under complex flow histories defined through the Lagrangian mapping proposed here as a means of rigorous testing. Additionally, the enormous datasets provided by sSAXS in the FFoRM could enable a data-driven “machine-learning” approach to the formulation of constitutive models on a purely mathematical basis, circumventing the need for formulating and solving accurate physical models. In this way, information about the structure under a wide range of flow histories could be used to train a predictive model that generates the structural response under some arbitrary flow history, enabling predictive design without the need for a physical model. Given that the flow histories probed in a sSAXS measurement can be tuned, one could build protocols such that new measurements can supplement regions of said predictive model that have limited information and improve its accuracy. Overall, the sheer size of the datasets collected by sSAXS in the FFoRM could enable a fundamental shift in the development of constitutive models for soft materials in flow.

V. CONCLUSIONS

In this work, we demonstrated a method, sSAXS in the FFoRM, for mapping the nanostructural response of material structure to a wide range of processing flows and demonstrated potential to “fingerprint” a soft material's microstructure under complex and tunable flow histories toward the development of process-structure-property relationships. The CNC and CNF dispersions used in this work are model materials to highlight these capabilities, which provide physical insight into the complex coupling between flow, intraparticle orientational order and interparticle structure. Asymmetry of the recorded flow fields of CNCs showed that interparticle alignment is dependent on the Lagrangian flow history, and not just the local flow field. By contrast, CNF dispersions are less homogeneous and show less history dependence in the alignment under the studied conditions.

The structural information contained in the collected SAXS pattern at each material point further enables a more detailed structural characterization than is available with other techniques. To highlight this, we developed and tested a simple analysis to assess the effect of flow on interparticle interactions by characterizing the degree of alignment at two different structural length scales, which revealed rich information and insight regarding the effect of interparticle interactions on the anisotropic structure of rodlike dispersions. For similar strain rate and flow types, CNCs align to a higher degree of intraparticle alignment than the CNFs. The inter- and intraparticle degrees of alignment have a constant proportionality that is invariant to the type of the flow or degree of alignment for flows with constant deformation rate. Based on the difference in magnitude of this proportionality constant between the CNFs and the CNCs, we propose the q -dependent anisotropy ratio $\alpha_{\text{low-}q}/\alpha_{\text{high-}q}$ as a simple, model-independent

metric whose magnitude differentiates whether the effects of interparticle structure on flow-induced orientational order are dominated by attractive or repulsive interparticle interactions. Overall, the well-defined flows under which material nanostructure is characterized opens a number of possibilities in the flow processing of soft materials, including inverse design schemes for flow histories to produce a particular microstructure, testing physical models for microstructure evolution under complex flows, and alternative data-driven approaches to the rheological modeling of complex fluids.

VI. EXPERIMENTAL METHODS

A. Materials

An aqueous dispersion of rodlike cellulose nanocrystals (University of Maine Process Development Center, Lot 2013-EPL-CNC-053) was used as a model shear-thinning fluid with minimal elasticity. D_r , 0 was adjusted through changing the solvent viscosity by mixing water and glycerol. We prepared the sample by adding 4 wt % of the dry, white CNC powder to the premixed solvent (90 wt % glycerol and 10 wt % MilliQ water) and ultrasonicated (700 W Fischer sonicator dismembrator) in an ice bath at 60% amplitude for 20 min in 40 cycles of 30 s on and 30 seconds off. A 1 wt % cellulose nanofiber dispersion was provided by RISE (Sweden) and prepared according to Wågberg *et al.* [45]. The 0.25 wt % dispersion was prepared by dilution with MilliQ water.

B. FFoRM fabrication and operation

FFoRM Devices consist of two outer plates squeezed around an inner plate containing the FFoRM geometry. Compared to the FFoRM geometry reported by Corona *et al.* [18], the FFoRM geometry reported in this work has smaller dimensions, which are indicated in Fig. 1. Additionally, several modifications were made to the sample environment to enable compatibility with sSAXS measurements. The outer plates were constructed out of poly(methyl methacrylate) and contain holes for Kapton windows to allow for x rays and visible light to pass through the device and for the connectors to inlet/outlet tubing. The inner plate was constructed out of titanium and the geometry was cut using a wire electrical discharge machine (EDM). The three plates were sealed together with sheets of double-sided tape. The device is controlled by varying the inlet and outlet flow rates into four of the eight channels with nMESYS syringe pumps (Cetoni GmbH), leaving the other four submerged in a container for fluid recirculation. Information on relating inlet/outlet flow rates to the generated flow types and deformation rates can be found in Corona *et al.* [18].

C. Particle-tracking velocimetry

Flows of the CNC dispersion in the FFoRM were experimentally determined using particle-tracking velocimetry (PTV) according to Ref. [18]. The dispersions were seeded with neutrally buoyant hollow glass spheres (10- μ m diameter, 300 ppm) and injected into the device's four inlet channels using two syringe pumps (pump: Harvard Apparatus PHD

2000, tubing: Saint-Gobain Versilon 2001) at different rates. The four additional outlets were immersed in a container of the test fluid. The outlet tubing was cut to similar length and immersed at similar height to avoid differences in pressure between outlet channels. A complementary metal-oxide semiconductor camera (Point Gray Gazelle 2.2 MP Mono Camera Link) with 12 \times total magnification and variable frame rate (from 1 to 280 fps) was focused on the center plane of the device geometry. Particle trajectories were determined from videos by stacking collected images with IMAGEJ.

D. Computational fluid dynamics simulations

CFD simulations were carried out with the COMSOL MULTIPHYSICS software package. Flow fields were generated from simulations for a generalized Newtonian fluid with the fluid density $\rho = 1.0$ g/mL and the strain-rate-dependent fluid viscosity (η) described by the Carreau model

$$\eta(|\mathbf{E}|) = \eta_0(1 + (\lambda|\mathbf{E}|)^2)^{\frac{n-1}{2}},$$

where $|\mathbf{E}|$ is the magnitude of the rate of strain tensor and $\eta_0 = 0.609$ Pa s, $\lambda = 0.276$ s, and $n = 0.839$ as a fit to the steady shear rheology of the 4 wt % CNC dispersion. The generalized Navier–Stokes and continuity equations were solved numerically for a 3D meshed representation of the geometry using a finite-element method in COMSOL MULTIPHYSICS. Constant-volume flow rate boundary conditions were specified at the ends of the channels corresponding to Q_1 and Q_2 , constant-pressure boundary conditions were specified at the ends of unlabeled channels, and no-slip boundary conditions were specified for all other walls.

To analyze Lagrangian trajectories, streamlines were generated from the simulations and chosen to match the desired trajectories measured with PTV. The velocity, flow-type parameter, and deformation rate were calculated along these streamlines. The strain at points (x_n) along a streamline was calculated from the velocity, U , as

$$\gamma = |\mathbf{E}|t = \int_{x_0}^{x_n} |\mathbf{E}|(x) \frac{dx}{U(x)} \approx \sum_{x=x_0}^{x_n} |\mathbf{E}|(x) \frac{\Delta x(x)}{U(x)},$$

where Δx is the distance between the point of interest and the previous point and $|\mathbf{E}|$ is the magnitude of the rate of strain tensor.

E. Scanning SAXS operation

Scanning SAXS (sSAXS) measurements were carried out at the cSAXS (X12SA) beamline of the Swiss Light Source (SLS) at the Paul Scherrer Institute (PSI) in Villigen PSI, Switzerland. The samples were scanned by a beam with a photon energy of 11.2 keV, which was defined by a fixed-exit double-crystal Si(111) monochromator, and focused to a 25×10 - μ m² beam size. A 2-m-long flight tube under vacuum was inserted between the sample and the detector to minimize air scattering and x-ray absorption. The sample-to-detector distance was 2.16 m, calibrated by silver behenate. A Pilatus 2M detector [46] (1475×1679 pixels, pixel size: 172×172 μ m²) was used to acquire 2D small-angle scattering patterns. Simultaneously, the transmitted beam was measured by the fluorescence of the used steel beamstop

mounted inside the flight tube. A raster scan was performed on a chosen sample area with a step size of $25 \times 25 \mu\text{m}^2$, and an exposure time of 0.1 s. Data processing was carried out using the “CSAXS SCANNING SAXS PACKAGE” developed by the CXS group, PSI, Switzerland [34]. The averaged scattering signal of the empty FFORM device was used as background. The background subtraction was followed by an orientation analysis, which was performed by the method described in detail in Ref. [34].

ACKNOWLEDGMENTS

The work was supported by the U.S. Department of Energy, Office of Science, Office of Basic Energy Sciences under Grant No. DE-SC0014127, the Chalmers Area of Advanced

Materials, the ForMAX pre-project financed by the Swedish Government and VR project (Grant No. 2018–06469: The FORMAX-portal - access to advanced X-ray methods for forest industry). International travel and fellowship support was provided by the NSF IRES Program: Cooperative for Advanced Materials in Energy-Related Applications (CAM-ERA), Award No. 1827034. The authors acknowledge Andy Weinberg at the University of California, Santa Barbara College of Engineering Machine Shop for assistance with device fabrication and Oscar Davidsson for his help with the beam-line experiments. We acknowledge the Paul Scherrer Institute, Villigen, Switzerland for provision of synchrotron radiation beamtime at the cSAXS beamline of the SLS.

P.T.C. and B.B. contributed equally to this work.

-
- [1] R. G. Larson, *The Structure and Rheology of Complex Fluids* (Oxford University Press, New York, 1999).
 - [2] Y. Diao, Y. Zhou, T. Kurosawa, L. Shaw, C. Wang, S. Park, Y. Guo, J. A. Reinspach, K. Gu, X. Gu, B. C. K. Tee, C. Pang, H. Yan, D. Zhao, M. F. Toney, S. C. B. Mannsfeld, and Z. Bao, *Nat. Commun.* **6**, 7955 (2015).
 - [3] B. B. Patel and Y. Diao, *Nanotechnology* **29**, 044004 (2018).
 - [4] M. K. Hausmann, P. A. Rühs, G. Siqueira, J. Läger, R. Libanori, T. Zimmermann, and A. R. Studart, *ACS Nano* **12**, 6926 (2018).
 - [5] S. Gantenbein, K. Masania, W. Woigk, J. P. W. Sesse, T. A. Tervoort, and A. R. Studart, *Nature (London)* **561**, 226 (2018).
 - [6] A. Sydney Gladman, E. A. Matsumoto, R. G. Nuzzo, L. Mahadevan, and J. A. Lewis, *Nat. Mater.* **15**, 413 (2016).
 - [7] R. G. Larson, *Rheol. Acta* **31**, 213 (1992).
 - [8] M. M. Denn, *Annu. Rev. Fluid Mech.* **33**, 265 (2001).
 - [9] P. Pakdel and G. H. McKinley, *Phys. Rev. Lett.* **77**, 2459 (1996).
 - [10] P. E. Arratia, C. C. Thomas, J. Diorio, and J. P. Gollub, *Phys. Rev. Lett.* **96**, 144502 (2006).
 - [11] R. B. Bird, R. C. Armstrong, and O. Hassager, *Dynamics of Polymeric Liquids* (John Wiley & Sons Inc., New York, 1987).
 - [12] M. Doi and S. Edwards, *The Theory of Polymer Dynamics* (Oxford University Press, New York, 1986).
 - [13] G. I. I. Taylor, *Proc. R. Soc.* **146**, 501 (1934).
 - [14] G. G. Fuller and L. G. Leal, *Rheol. Acta* **19**, 580 (1980).
 - [15] B. J. Bentley, L. G. Leal, B. J. Bentley, and L. G. Leal, *J. Fluid Mech.* **167**, 241 (1986).
 - [16] F. Pignon, A. Magnin, J.-M. Piau, and G. G. Fuller, *J. Rheol.* **47**, 371 (2003).
 - [17] J. S. Lee, R. Dylla-Spears, N. P. Teclemariam, and S. J. Muller, *Appl. Phys. Lett.* **90**, 074103 (2007).
 - [18] P. T. Corona, N. Ruocco, K. M. Weigandt, L. G. Leal, and M. E. Helgeson, *Sci. Rep.* **8**, 15559 (2018).
 - [19] H. A. Stone, B. J. Bentley, and L. G. Leal, *J. Fluid Mech.* **173**, 131 (1986).
 - [20] V. Lutz-Bueno, J. Zhao, R. Mezzenga, T. Pfohl, P. Fischer, and M. Liebi, *Lab Chip* **16**, 4028 (2016).
 - [21] M. E. Brennich, J. F. Nolting, C. Dammann, B. Nöding, S. Bauch, H. Herrmann, T. Pfohl, and S. Köster, *Lab Chip* **11**, 708 (2011).
 - [22] L. Geng, N. Mittal, C. Zhan, F. Ansari, P. R. Sharma, X. Peng, B. S. Hsiao, and L. D. Söderberg, *Macromolecules* **51**, 1498 (2018).
 - [23] K. M. O. Håkansson, A. B. Fall, F. Lundell, S. Yu, C. Krywka, S. V. Roth, G. Santoro, M. Kvick, L. Prah Wittberg, L. Wågberg, and L. D. Söderberg, *Nat. Commun.* **5**, 4018 (2014).
 - [24] T. Rosén, R. Wang, C. Zhan, H. He, S. Chodankar, and B. S. Hsiao, *Phys. Rev. E* **101**, 032610 (2020).
 - [25] A. P. R. Eberle and L. Porcar, *Curr. Opin. Colloid Interface Sci.* **17**, 33 (2012).
 - [26] A. Bharati, S. D. Hudson, and K. M. Weigandt, *Curr. Opin. Colloid Interface Sci.* **42**, 137 (2019).
 - [27] E. J. Hinch and L. G. Leal, *J. Fluid Mech.* **71**, 481 (1975).
 - [28] E. J. Hinch and L. G. Leal, *J. Fluid Mech.* **76**, 187 (1976).
 - [29] J. K. G. G. Dhont and W. J. Briels, *Colloids Surf. A: Physicochem. Eng. Asp.* **213**, 131 (2003).
 - [30] C. Lang, J. Kohlbrecher, L. Porcar, A. Radulescu, K. Sellinghoff, J. K. G. Dhont, and M. P. Lettinga, *Macromolecules* **52**, 9604 (2019).
 - [31] A. J. Szeri, W. J. Milliken, and L. G. Leal, *J. Fluid Mech.* **237**, 33 (1992).
 - [32] B. Weyerich, J. Brunner-Popela, O. Glatter, J. Brunner-Popela, and O. Glatter, *J. Appl. Crystallogr.* **32**, 197 (1999).
 - [33] See Supplemental Material at <http://link.aps.org/supplemental/10.1103/PhysRevMaterials.6.045603> for rheological characterization of test fluids, equilibrium SAXS measurements of test fluids, and details on nonequilibrium SAXS analysis.
 - [34] O. Bunk, M. Bech, T. H. Jensen, R. Feidenhans'l, T. Binderup, A. Menzel, and F. Pfeiffer, *New J. Phys.* **11**, 123016 (2009).
 - [35] P. T. Corona, K. S. Silmore, R. Adkins, C. Lang, M. P. Lettinga, J. W. Swan, L. G. Leal, and M. E. Helgeson, *Phys. Rev. Materials* **5**, 065601 (2021).
 - [36] B. H. Zimm, *J. Chem. Phys.* **14**, 164 (1946).
 - [37] I. Usov, G. Nyström, J. Adamcik, S. Handschin, C. Schütz, A. Fall, L. Bergström, and R. Mezzenga, *Nat. Commun.* **6**, 7564 (2015).
 - [38] M. Doi and S. F. Edwards, *J. Chem. Soc. Faraday Trans. 2 Mol. Chem. Phys.* **74**, 560 (1978).
 - [39] I. Teraoka, N. Ookubo, and R. Hayakawa, *Phys. Rev. Lett.* **55**, 2712 (1985).

- [40] Y.-G. Tao, W. K. den Otter, J. K. G. Dhont, and W. J. Briels, *J. Chem. Phys.* **124**, 134906 (2006).
- [41] H. Oguzlu, C. Danumah, and Y. Boluk, *Curr. Opin. Colloid Interface Sci.* **29**, 46 (2017).
- [42] K. Uetani and H. Yano, *Langmuir* **28**, 818 (2012).
- [43] H. Fukuzumi, R. Tanaka, T. Saito, and A. Isogai, *Cellulose* **21**, 1553 (2014).
- [44] L. M. Walker and N. J. Wagner, *Macromolecules* **29**, 2298 (1996).
- [45] L. Wågberg, L. Winter, L. Ödberg, and T. Lindström, *Colloids Surf.* **27**, 163 (1987).
- [46] P. Kraft, A. Bergamaschi, C. Broennimann, R. Dinapoli, E. F. Eikenberry, B. Henrich, I. Johnson, A. Mozzanica, C. M. Schlepütz, P. R. Willmott, and B. Schmitt, *J. Synchrotron Radiat.* **16**, 368 (2009).